



Architecting the AuPt alloys for hydrazine oxidation as an anolyte in fuel cell: Comparative analysis of hydrazine splitting and water splitting for energy-saving H₂ generation



Yiseul Yu ^{a,1}, Seung Jun Lee ^{b,1}, Jayaraman Theerthagiri ^{a,1}, Yerryeong Lee ^{a,b}, Myong Yong Choi ^{a,b,*}

^a Department of Chemistry (BK21 FOUR), Research Institute of Natural Sciences, Gyeongsang National University, Jinju 52828, Republic of Korea

^b Core-Facility Center for Photochemistry & Nanomaterials, Gyeongsang National University, Jinju 52828, Republic of Korea

ARTICLE INFO

Keywords:

Pulsed laser irradiation
Ultrasoundchemical process
AuPt alloy
Hydrazine oxidation reaction
Energy-saving H₂ fuel production
Overall hydrazine and water splitting

ABSTRACT

Replacing the kinetically sluggish anodic oxygen evolution reaction (OER) with hydrazine (N_2H_4) oxidation reaction (HzOR) could be the effective approach for achieving energy-saving hydrogen (H_2) fuel production in a water electrolyzer system. Thus, developing the efficient HzOR electrocatalysts, combined with the cathodic H_2 evolution reaction (HER) is of vital importance for the high-rate H_2 fuel generation as well as for the advancement of a N_2H_4 fuel cell. Herein, we utilized a facile integrated process of pulsed laser irradiation and sonochemical process to synthesize AuPt alloys by the irradiation of laser to a mixture of Au/Pt solution in methanol/DI water in varied proportions. The AuPt alloy plays a key role in the chemisorption of N_2H_4 on its surface, forming a dative bond involving electrons of the lone pair of nitrogen in N_2H_4 and empty orbitals of Pt in the alloy, indicating its high intrinsic activity against HzOR. The optimal composition of Au1Pt8 electrode demonstrates outstanding characteristics of HER with an ultralow overpotential of 26 mV at 10 mA cm⁻² in alkaline medium while requiring 502 mV to attain 10 mA cm⁻² for HzOR in 0.5 M N_2H_4 /1.0 M KOH electrolyte. In addition, the assembled overall N_2H_4 splitting electrolyzer cell using Au1Pt8 alloys as both anode and cathode requires cell voltage of only ~0.172 V at 10 mA cm⁻² with tremendous stability over 10 h, which is much lower than the voltage of 1.773 V required for the overall water splitting electrolyzer. The present study validates the feasibility of AuPt alloys for stimulating N_2H_4 fuel cells in the future to achieve both electrical energy generation and high-rate H_2 fuel production.

1. Introduction

The growing concern about environmental problems and energy crises due to the fossil fuels depletion has prompted even more study into clean and renewable energy resources. H_2 is regarded as the primary replacement energy carrier for fossil fuels because of its environmental friendliness and high gravimetric energy density [1–7]. Industrial H_2 is mostly produced by a catalytic steam reforming process that requires high pressure and accessibility of hydrocarbons with the discharge of a high amount of CO₂ greenhouse gases. Therefore, this catalytic steam process is obviously unsuitable for future sustainable progress, as well as for small-scale H_2 production on-site for specific

applications [8–10]. Because of the pollution-free process and inexhaustibility of the source materials, electrocatalytic overall water splitting (OWS), which comprises of two-half cell electrochemical reactions: cathodic HER and anodic OER, has been regarded as a capable and convenient pathway for H_2 [11–14]. However, the increase in energy efficiency from OWS is strongly hindered by the sluggish electrode reaction kinetics, in particular the high theoretical potential of OER (1.23 V vs RHE). Even though sophisticated electrocatalysts for bifunctional HER and OER have been widely reported, in a practical water electrolyzer, the cell voltage input of ~1.6–2.0 V is still required for OWS [1]. Subsequently, the approaches for replacing OER with other kinetically favorable oxidation reactions are essential to achieve the remarkable

* Corresponding author at: Department of Chemistry (BK21 FOUR), Research Institute of Natural Sciences, Gyeongsang National University, Jinju 52828, Republic of Korea.

E-mail address: mychoi@gnu.ac.kr (M.Y. Choi).

¹ These authors contributed equally to this work

potential of H₂ production. The HzOR, which is favorable from this perspective and requires a potential of only -0.33 V vs RHE, significantly lower than that of OER, has recently been offered as an alternate choice for energy-saving techniques in a bright context [15–18]. Aside from the ultralow cell voltage desires for overall hydrazine splitting (OH₂S) electrolyzer, the membrane-free design can be applied in the commercial applications of the N₂H₄ electrolyzer as the only by-product of inert N₂ gas at the anode rather than the explosive H₂/O₂ mixture in the OWS electrolyzer [1,15]. HzOR has other advantages of high power, energy density, and zero CO₂ emission [15,19]. Recently, it was discovered that N₂H₄ in alkali solution-acid hybrid fuel cells with various catalytic electrode materials significantly improved the ability to deliver electrical energy upon H₂ generation. The design of highly effective electrocatalysts with good stability is critical for developing a high-performance HzOR-assisted electrolyzer or N₂H₄/acid hybrid cell [8,20–23]. More recently, pioneering research has demonstrated that creating alloy or bimetallic nanocatalytic materials could be an effective strategy for modulating the surface-active sites and electronic structure of electrocatalysts simultaneously [24,25]. Electronic states are extremely susceptible to changes during hybridization of various metal d-states due to electron transfer among the metals [26,27]. Among the several bimetallic catalytic systems, the alloying of Au with Pt has received considerable attention due to the increased electrocatalytic activity of Pt combined with Au metal as a result of effective electronic and synergistic effects [28]. Thus, the electronic effect is caused by the d-band shift of Pt in AuPt alloy, whereas the synergistic effect implies that Au and Pt in the alloys show proportional competencies and improve catalytic characteristics. These catalyst functionalities not only support each constituent's intrinsic electrocatalytic activities but also provide superior multifunctional electrochemical activities ascribed to the interfacial catalytic synergistic effect, which has been controlled by innovative synthetic techniques [29,30].

Various innovative synthetic techniques are widely utilized for the fabrication of noble alloy and bimetallic nanocatalysts. In this study, we employed an integrated process of pulsed laser irradiation (PLI) and sonochemical process to synthesize AuPt alloys by the irradiation of laser to a Au/Pt mixture of solution in methanol/DI water in varied proportions. PLI synthesis is hypothetically advantageous compared with all other synthesis techniques due to the high surface-active and impurity-free surface of the nanomaterials, as well as the absence of any external reducing agents [31]. PLI synthesis has additional advantages such as speed, simplicity, and cost-effectiveness [32–34]. PLI materials were electrostatically stable and did not require any external purification. The solvents decompose during irradiation of the reaction mixture, yielding various free radicals, solvated electrons, etc., where the generated H[·] radicals act as powerful reducing agents in the metal solution, reducing the metal salts into resultant metal nanoparticles (NPs) [24]. Furthermore, the integration of the PLI process with the sonochemical process dramatically increases the number of H[·] radicals via the ultrasonic cavitation phenomena, resulting in the enhanced product yield, uniformly distributed particles, and fast reaction time. Experimental results reveal that the appropriate proportion ratio of Au and Pt in AuPt alloys efficiently improves electron integration and optimizes the catalytic reactions energy barriers, resulting in a trifunctional electrocatalytic activity toward the HzOR, HER, and OER. More impressively, the constructed HzOR-assisted electrolyzer with Au1Pt8 alloys requires cell voltage of only ~ 0.172 V to deliver 10 mA cm⁻², which is significantly lower than the ~ 1.773 V required by the OWS electrolyzer. This study demonstrates the feasibility of AuPt alloys for stimulating N₂H₄ fuel cells to deliver both electrical energy generation and H₂ fuel consistently.

2. Experimental part

2.1. Materials

Gold (III) chloride trihydrate ($\geq 99.9\%$, HAuCl₄·3H₂O), potassium tetrachloroplatinate (II) ($\geq 98\%$, K₂PtCl₆), potassium hydroxide ($\geq 93\%$, KOH extra pure flakes), methanol solvent (HPLC grade), and hexadecyltrimethylammonium chloride ($\geq 99.8\%$, CTAC) were purchased from Daejung Chemicals, Korea. Nafion perfluorinated resin (5 wt %) solution was obtained from Sigma-Aldrich, USA. Carbon black (Vulcan XC-72) powder was acquired from Cabot, USA. Hydrazine hydrate ($> 98\%$, N₂H₄ H₂O) was procured from TCI, Japan. All chemicals utilized without additional purification.

2.2. Synthesis of AuPt alloys with various compositions

The various compositions of AuPt alloys were synthesized using PLI coupled with the sonochemical process. First, the stock solution of HAuCl₄·3H₂O and K₂PtCl₆ of 2.5 mM each was prepared using methanol and DI water. Using methanol solvent, various reaction mixtures of HAuCl₄·3H₂O and K₂PtCl₆ stock solution in the ratios 8:1, 4:1, 1:1, 1:4, and 1:8 were prepared to maintain a total concentration of 0.1875 mM per 12 mL. Then, 0.0192 mg of CTAC was added to this reaction mixture as a surfactant. Thereafter, the reaction mixture was irradiated for 10 min using the pulsed laser (Nd:YAG, Surelite II-10) in a vertical form under a continuously ultrasonic wave (Rainbow SD-350 H, power: 100-W and frequency: 40-kHz). The optimized conditions of pulsed laser were a laser power of 120 mJ, a wavelength of 532 nm, and a pulse width of 7 ns at a repetition rate of 10 Hz. Finally, the resulting colloidal solution was collected and 2 mg of carbon black was added under ultrasonic waves for 30 min for the good distribution of AuPt alloys. Subsequently, AuPt alloys were obtained via centrifugation, washed well with methanol to eliminate unreacted residue, and dried at an ambient temperature. The detailed formation mechanism of AuPt alloys was discussed in Section S.T1 of Supplementary Information.

2.3. Characterization techniques

The purity and structure formation of the materials were examined using a powder X-ray diffractometer (XRD) (Bruker, D8-Advance A25 instrument, Germany) with Cu-K α ($\lambda = 1.5405$ Å) radiation. Morphologies of the materials and elemental composition were analyzed using field emission scanning electron microscopy (FE-SEM, TESCAN CLARA, Czech Republic), high-resolution transmission electron microscopy (HR-TEM, FEI Technai G2 spirit TWIN, USA) equipped with energy-dispersive X-ray spectroscopy (EDX, Talos F200X with Super-X: 4 SDD detectors), and inductively coupled plasma optical emission spectrometer (ICP-OES, PerkinElmer, Optima 8300DV, USA). Surface compositions of the materials were characterized using X-ray photoelectron spectroscopy (XPS, NEXSA, Thermo Fisher Scientific, USA), and the Raman spectra were conducted via Raman microscope (LabRAM, Horiba Jobin Yvon, Model-HR800). The zeta potentials for the various compositional ratios of AuPt nanoalloys in colloidal suspensions were measured by dynamic light scattering using Zeta potential analyzer (Malvern NANO ZS instrument, UK). Fourier-transform infrared spectroscopy was analyzed using Nicolet iS5 FT-IR spectrometer (Thermo scientific, USA). The specific surface area and pore volume of the optimal AuPt alloy were investigated using a BELSORP-mini II BET surface area analyzer (BEL, Japan). Gas geometrography (Master GC, DANI) equipped with a thermal conductivity detector (TCD), HP-MOLSIVE column, and N₂ as carrier gas was utilized to detect the produced H₂ gas sampled by a gas-tight syringe.

2.4. Electrochemical measurements

All electrochemical tests were carried out using a CHI708E

electrochemical analyzer (CH Instruments, Inc., USA). In a characteristic three-electrode set-up, as-synthesized AuPt materials coated on carbon cloth (CC, area $\sim 1 \times 1 \text{ cm}^2$) as the working electrode, graphite rod and Hg/HgO electrode filled with 1.0 M KOH were employed as counter and reference electrode, respectively. The fabrication procedure for the working electrode is as follows: the electrocatalyst ink was prepared by dispersing 1 mg of as-synthesized AuPt alloy in a solution composed of 45 μL of deionized water, 45 μL of ethanol, and 10 μL of 5 wt % Nafion resin solution under constant sonication for 30 min. Then, the catalyst ink was drop cast on the surface of CC and dried at 60 $^\circ\text{C}$ for 1 h. Before the catalyst coating, the CC was activated by immersing in 0.5-M sulfuric acid for 24 h, which can make CC more hydrophilic. All potential recorded with Hg/HgO reference electrode were converted to RHE reference scale according to the equation of $E_{\text{RHE}} = E_{\text{Hg/HgO}} + 0.059 \text{ pH} + E^\circ_{\text{Hg/HgO}}$, where, $E_{\text{Hg/HgO}}$ is the experimental potential, pH refers to the electrolyte pH (1.0-M KOH ~ 14), and $E^\circ_{\text{Hg/HgO}}$ is the potential of typical Hg/HgO reference electrode $\sim 0.098 \text{ V}$. HER and OER

measurements were performed in 1.0-M KOH electrolyte, whereas HzOR was carried out in 0.5-M N_2H_4 in 1.0-M KOH solution. The polarization curves of the fabricated electrocatalysts were measured using the linear sweep voltammetry (LSV) technique at a scan rate of 5 mV s^{-1} .

The Tafel slope was estimated by fitting the linear part of the Tafel plots obtained using LSV curves, by plotting the overpotential (η) versus the log of current density ($\log(j)$) according to the Tafel equation $\eta = b \log(j) + a$, where, b is the Tafel slope and a is denoted as the Tafel constant. Electrochemical impedance spectroscopy (EIS) tests were recorded in the frequency ranges from 0.1 Hz to 100 kHz at an AC voltage of 5 mV. The cyclic voltammetry (CV) curves were collected at various scan rates between 10 and 100 mV s^{-1} in a non-Faradaic region of the selected potential window from 0.1 to 0.2 V vs Hg/HgO in 1.0-M KOH electrolyte to estimate the double-layer capacitance (C_{dl}) values. The C_{dl} values are the slope values obtained by the linear relationships between half of the difference in anodic and cathodic peak current densities ($\Delta J/2 = j_a - j_c/2$) against scan rates, which can be expressed in

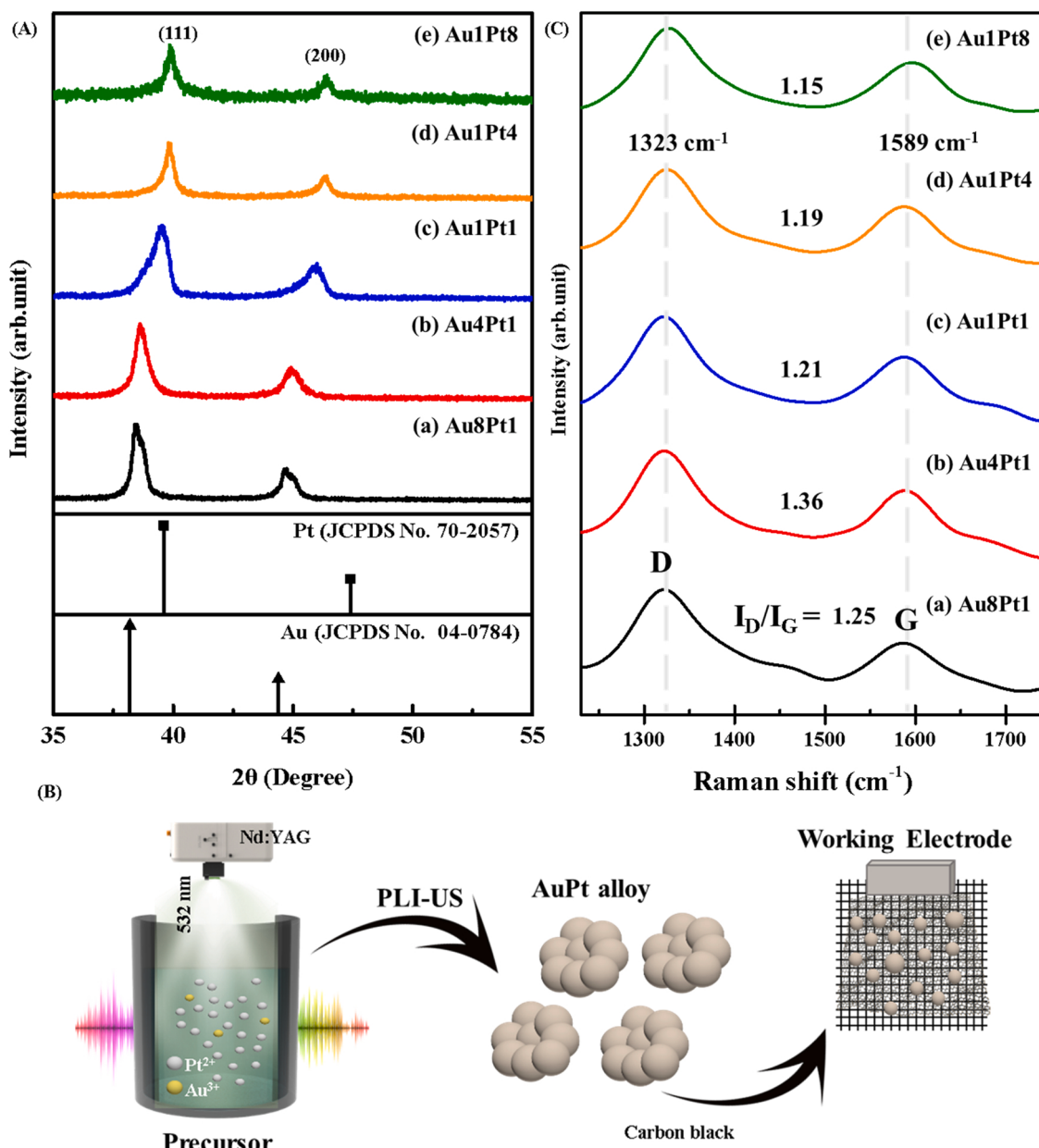


Fig. 1. (A) XRD patterns, (B) schematic design of the synthesis of AuPt alloys for energy-saving H_2 generation, and (C) Raman spectra of the synthesized AuPt alloys of various compositions.

the equation $C_{dl} = d(\Delta j)/2d\nu$, where ν is the scan rate [27,35].

The electrochemical active surface area (ECSA) can be calculated from C_{dl} , according to the following equation: $ECSA = C_{dl}/C_s$, where C_s is the specific capacitance of flat CC substrate $\sim 88 \text{ mF cm}^{-2}$ [36].

Turnover frequency (TOF, s^{-1}) was measured and estimated using the equation $TOF = j/2nF$, where j is the current density, 2 is the number of electrons involved in the HER (in case OER is 4 and HzOR is 4), n is the number of active sites, and F is the Faraday constant ($96,485.3329 \text{ C mol}^{-1}$). The number of active sites ($n, \text{ mol cm}^{-2}$) was calculated according to the formula of $n = Q_s/F$, where Q_s is the surface charge density that can be obtained by integrating the charge of the full CV curve and its half of the value referred to as Q_s . For the calculation of n , the CV measurements were carried out in the potential window of $-0.075\text{--}0.65 \text{ V vs RHE}$ at 50 mV s^{-1} in 1.0-M KOH solution [1,37].

Besides, the OWS (HER and OER) and OHzS (HER and HzOR) measurements were carried out in a single compartment with two-electrode cells by utilizing Au1Pt8 coated on CC as both the cathode and anode. The 1.0-M KOH was used as an electrolyte for OWS, and $0.5\text{-M N}_2\text{H}_4$ in 1.0-M KOH was used as an electrolyte for OHzS. The advantage of a membrane-less single compartment electrolytic cell is to simplify the electrolytic process by eliminating the membrane and reducing the operation cost. Furthermore, the internal resistance can decrease and enhance hydrogen generation.

3. Results and discussion

3.1. Structural analysis

The crystalline purity and phase of the synthesized AuPt alloys of various compositions were evaluated using a powder XRD, and the observed diffraction patterns are shown in Fig. 1A. As noticed from Fig. 1A, that the detected diffraction peaks for all AuPt alloy compositions were located between two standard monometallic peaks – Au (JCPDS file # 04–0784, 20 peaks at 38.19° and 44.39°) and Pt (JCPDS file: 70–2057, 20 peaks at 39.77° and 46.25°) [27]. The observed two main diffraction peaks of Au8Pt1 at 38.55° and 44.79° were indexed as the crystal faces of (111) and (200) planes for face-centered cubic structures of AuPt alloys (Fig. 1A(a)). The noticeable shifts in the diffraction peaks are observed toward standard Pt peaks upon increasing the concentration ratio of Pt in AuPt from Au8Pt1 to Au1Pt8, as shown in Fig. 1A(a) – (e). It is probably due to the reduction of $\text{HAuCl}_4 \cdot 3 \text{ H}_2\text{O}$ and K_2PtCl_6 to Au and Pt elements first, and then, Au and Pt atoms diffused each other into the Au/Pt crystal to expand or contract the lattice of monometallic structures with changes in composition [38]. Concurring to Vegard's law, shifts in the diffraction peak of nanoalloys either decrease or increase reliant on the element proportion ratio [24]. The average size, strain, and interplanar distance (d-spacing) of the synthesized samples were calculated using high intensity (111) diffraction peak by Scherrer's, Williamson–Hall, and Bragg's equations, respectively [27] (Table S1). The results obtained are listed in Table S1, which shows that the lattice parameters for the synthesized cubic structures of AuPt were estimated in the range of ~ 4.036 to $\sim 3.917 \text{ \AA}$, which is between the standard Au (4.078 \AA) and Pt (3.923 \AA), indicating the formation of AuPt alloys (Fig. S1). The growth of crystallite size also varies depending on the proportion of the Au and Pt in AuPt alloys (Table S1), with similar crystallite size for alloys Au8Pt1 (13.69 nm) and Au1Pt8 (13.54 nm), possibly due to the close atomic radius of Au and Pt. The localized lattice strain is expected to rise when crystallite size decreases, and the high value of lattice strain can improve the electrochemical performance of the catalyst [39]. The lattice strain is initiated by the atoms deviation from the original position due to the structural defects, i.e., grain boundaries, dislocation arrays, twins, and stacking faults, which can alter the diffraction peaks to compress or expand. The results in Table S1 suggest that the strain effect has no significant influence on the catalytic performance of the synthesized AuPt alloys and the synergistic and electronic effects may influence the surface-active sites of

the electrocatalysts. As seen in the schematic illustration of AuPt alloy synthesis (Fig. 1B) and Section 2.2, we added 2 mg of carbon black uniformly to all the samples during synthesis to attain well distribution of AuPt alloys, which was confirmed using the Raman analysis. The Raman spectra of synthesized AuPt alloys of various compositions are shown in Fig. 1C, where there are two main peaks at ~ 1323 and $\sim 1589 \text{ cm}^{-1}$, which resemble to defect (D) and graphite (G) bands of carbon structure, respectively [40]. The resulting D and G bands are associated with the lattice mismatch defects of carbon and E_{2g} mode produced by C–C sp^2 bonds of stretching vibrations, proving the presence of carbon in AuPt alloys. Moreover, the Raman spectra show an almost similar shape with a ratio of D/G band intensities (I_D/I_G) of $\sim 1.25 \pm 0.1$, indicating the same amount of carbon present in all compositions of AuPt alloys.

The morphological surface structure of various AuPt alloy compositions was evaluated using FE-SEM, and the obtained images are shown in Fig. S2. The FE-SEM surface images show that all the compositions of AuPt alloys form spherical-shaped nanoalloys, and the particle size tends to decrease as the Pt fraction increases (Fig. S2). Well-connected states of surface morphological structures can play a crucial role in improving electrocatalytic performances [41]. The purity and existence of Au and Pt elements in the AuPt alloys were confirmed by EDX-mapping, and the resultant images are provided in the inset of corresponding FE-SEM images (Fig. S2), and the EDX elemental spectrum of an optimal Au1Pt8 alloy is shown in Fig. S2f. Besides, the elemental proportion of various AuPt nanoalloys was detected using the EDX and ICP-OES. The elemental proportion results in Table S2 reveal that the composition of Au8Pt1, Au4Pt1, Au1Pt1, Au1Pt4, and Au1Pt8 agrees well with the results of EDX and ICP-OES. The HR-TEM was further utilized to investigate the surface structure, dispersion, and particle size of AuPt nanoalloys. HR-TEM images also revealed the formation of spherically shaped AuPt nanoalloys, and the average particle size decreases with the increasing proportion of the Pt element, as exposed in Fig. 2a–e. The average size of the Au8Pt1 alloy ranges from 15 to 25 nm, whereas the size of the Au1Pt8 alloy ranges from 5 to 8 nm. The observed d-spacing value of 2.27 \AA (0.227 nm) corresponds to the (111) plane of AuPt alloys (inset of Fig. 2f), and this result is well matched with the XRD studies. In addition, as mentioned in Section 2, carbon black was added during the synthesis for good dispersion of AuPt nanoalloys, which was confirmed using HR-TEM analysis (Fig. S3). In addition, the STEM with cross-sectional composite line profiles and EDX mapping of an optimal Au1Pt8 nanoalloy with carbon support (Fig. 2g-i to g-vi) revealed the co-existence of Au and Pt, confirming the formation of AuPt alloy. Besides, the zeta potential for the synthesized various compositional ratios of AuPt nanoalloys was examined by dynamic light scattering. The zeta potential value is directly related to the electrostatic interactions such as attraction or repulsion among the Au and Pt, and the surface charge of the catalytic nanoparticles [24]. Commonly, materials above 25 mV or less than -25 mV zeta potential values are considered stable materials [24]. The estimated zeta potential value of Au1Pt8 is around -30.5 mV , which is lower than that of Au1Pt4 (-22 mV), Au1Pt1 (-23 mV), Au4Pt1 (-14.2 mV), and Au8Pt1 (-10.3 mV) which indicates that the improved stability of an optimal Au1Pt8 alloy with a low zeta potential value.

To further inspect the oxidation states, surface composition, and electronic structure of the synthesized AuPt nanoalloys, a core-level XPS study of AuPt samples was performed, and the resultant spectra are provided in Fig. 3. The overall survey XPS spectrum for all the compositions of AuPt nanoalloys confirmed the presence of Au, Pt, and C elements (Figs. S4 and Fig. 3a–c). As displayed in Fig. 3a, the C 1s spectra of all the AuPt alloys exhibit a major peak at 284.2 eV with the same intensity confirming the uniform amount of carbon in all the nanoalloy samples. The Au 4f and Pt 4f spectra reveal the change in peak intensity as well as peak shifts (change in binding energy, ΔBE) according to the proportion of the Au and Pt elements in the AuPt nanoalloys (Fig. 3(b and c) and Table S3). The ΔBE of 4 f peak implies the charge transfer process between Au and Pt through electron interactions that do not

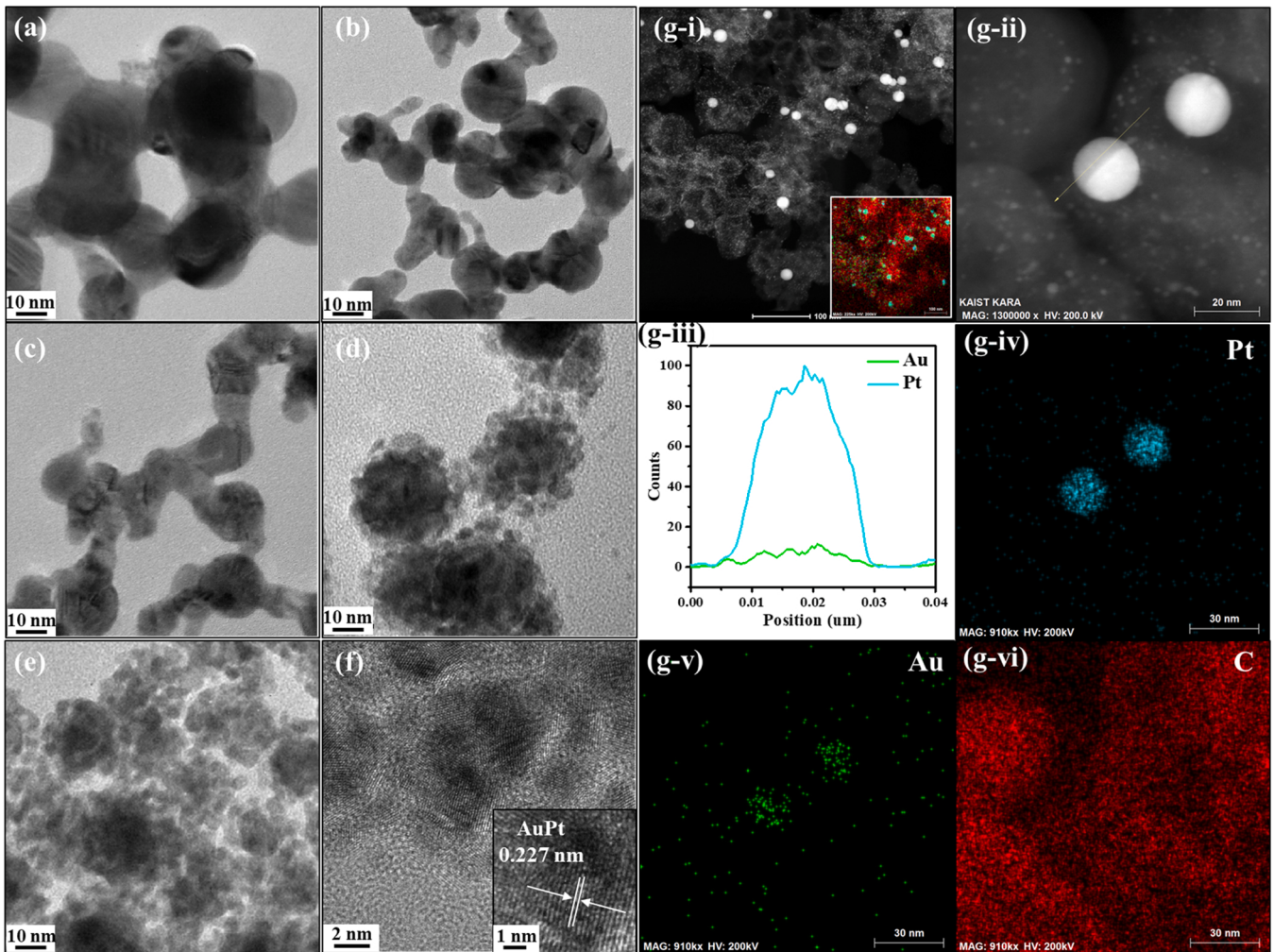


Fig. 2. (a–e) HR-TEM images of Au8Pt1, Au4Pt1, Au1Pt1, Au1Pt4, and Au1Pt8 alloys; (f) HR-TEM image of an optimal Au1Pt8 alloy with high magnification and inset shows the d-spacing value of 0.227 nm corresponds to the (111) plane of AuPt alloy; and (g–i) STEM images of Au1Pt8 alloy (inset shows EDX mapping) and (g–ii to g–vi) zoomed view of STEM image of g–i with cross-sectional composite line profiles and EDS mapping of an optimal Au1Pt8 alloy with carbon support.

correspond to their Pauling electronegativity scale, i.e., 2.28 for Pt and 2.54 for Au [42,43]. According to the nominal electronic configuration of Au ([Xe] 4 f¹⁴5d¹⁰6 s¹) and Pt ([Xe] 4 f¹⁴5d⁹6 s¹), Au 6 s requires an electron to achieve completely filled s-orbital. On the basis of the electronegativity, an electron transfer occurs from 5d of Pt to 6 s of Au, altering the electronic configuration as Au ([Xe] 4 f¹⁴5d¹⁰6 s²) and Pt ([Xe] 4 f¹⁴5d⁸6 s¹), resulting in d-charge depletion in Pt. To maintain this d-charge depletion and electroneutrality, an electron redistribution process takes place via s-d hybridization resulting an empty 6 s orbital in Pt with a change in electron configuration as Au ([Xe] 4 f¹⁴5d¹⁰6 s¹) and Pt ([Xe] 4 f¹⁴5d¹⁰6 s⁰). This electron redistribution clearly explains the anomalous behavior and is well correlated with the observed ΔBE [44]. Furthermore, the detailed deconvoluted core spectra of C 1 s, Au 4 f, and Pt 4 f for the optimal Au1Pt8 nanoalloy are shown in Fig. 3d–f. The major peak of C 1 s at 284.2 eV was deconvoluted into two peaks at 284.12 and 284.98 eV, which are attributed to the hybridization of sp² and sp³ carbons, respectively. Meanwhile, the Au 4 f XPS core spectra in Fig. 3e show a pair of peaks at 87.28 and 83.58 eV allotted to Au 4 f_{5/2} and Au 4 f_{7/2}, respectively, which can be attributed to the metallic Au⁰ [27,45]. As displayed in Fig. 3f, the core-level spectra of Pt 4 f exhibit two major peaks centered at 74.18 and 70.88 eV ascribed to the Pt 4 f_{5/2} and Pt 4 f_{7/2} spin-orbit splitting of Pt⁰, respectively. An additional two weakest peaks were detected by deconvolution, with centers at 75.35 eV (Pt 4 f_{5/2}) and 72.08 eV (Pt 4 f_{7/2}) associated with Pt²⁺ species (Fig. 3f) [38]. Thus, the formation of Pt²⁺ on the surface of AuPt alloys may occur

during the charge neutrality process. Therefore, the XPS analysis results are well reliable with the XRD, HR-TEM, EDX, and STEM remarks, indicating the formation of an AuPt alloy structure and good integration of Au and Pt metal.

3.2. Electrocatalytic HER

The electrocatalytic activity of the synthesized AuPt samples tested for HER in 1.0-M KOH solution using a conventional three-electrode setup and the resulting LSV polarization curves measured at 5 mV s⁻¹ are depicted in Fig. 4a. First, the Au/Pt ratio effect on HER performance was investigated. Au1Pt8 has been shown to exhibit exceptional electrocatalytic HER activity with a small η of 26 mV to attain 10 mA cm⁻², which is much lower than Au1Pt4 (135 mV), Au1Pt1 (172 mV), Au4Pt1 (403 mV), and Au8Pt1 (535 mV), as represented in Fig. 4b. Thus, the enhanced electrocatalytic activity of Au1Pt8 toward HER can be ascribed to the chemical and electronic effect caused by electron redistribution between Au and Pt in AuPt alloy. Subsequently, the positive synergistic effect between the Au and Pt alloying and added carbon black can also contribute to the conductivity for the good dispersion of the AuPt alloy [46]. The derived Tafel plots from the cathodic LSV curves are depicted in Fig. 4c, where the Au1Pt8 electrocatalyst displays a much lower Tafel slope of 88 mV dec⁻¹ than Au1Pt4 (126 mV dec⁻¹), Au1Pt1 (149 mV dec⁻¹), Au4Pt1 (247 mV dec⁻¹), and Au8Pt1 (280 mV dec⁻¹), signifying the superior electrocatalytic HER kinetics of Au1Pt8.

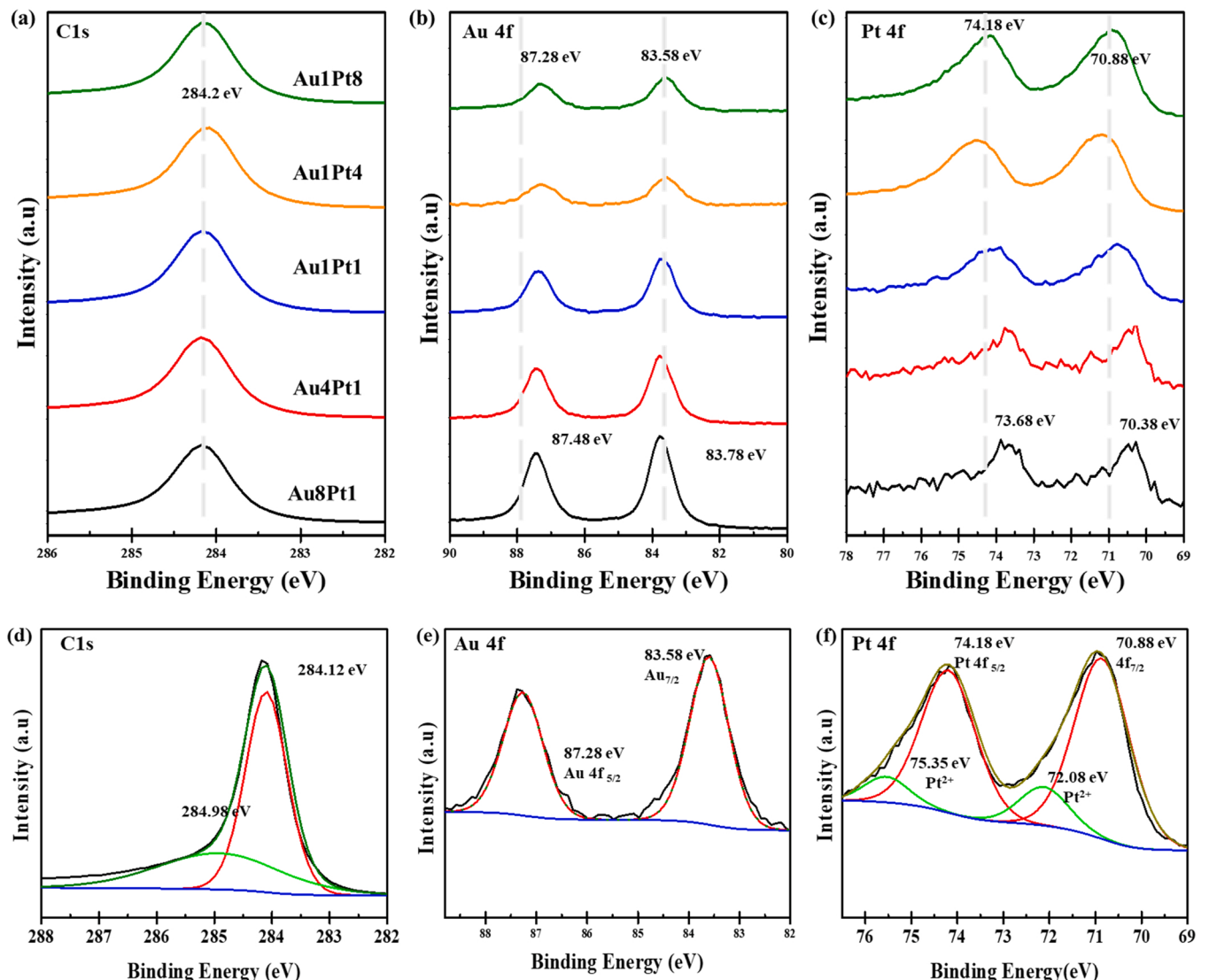
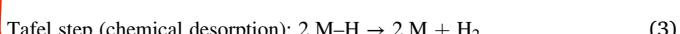
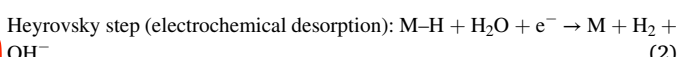
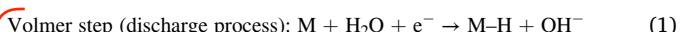


Fig. 3. (a–c) XPS core spectra of C 1 s, Au 4 f, and Pt 4 f obtained for the synthesized various compositions of AuPt alloys and (d–f) deconvoluted core level spectra of C 1 s, Au 4 f, and Pt 4 f of the optimized Au1Pt8 alloy.

As shown in Table S4, Au1Pt8 outperforms most recently reported electrocatalysts in terms of HER performance.

The Tafel analysis is usually utilized to understand the HER reaction mechanism. According to a previous report by Li et al. [15], the reaction mechanism of an electrocatalyst in an alkaline solution can be as follows (Eqs. (1)–(3)):



where M denotes the active surface site of the electrocatalyst and M-H states the H_2 atom adsorbed (H_{ads}) on the active surface site of the electrocatalyst. Based on the three steps mentioned above, the two likely HER mechanisms are the Volmer-Tafel and Volmer-Heyrovsky routes. Both the mechanisms are shared by the Volmer step (first step), which differ only by the desorption step, either chemical desorption (Tafel step) or electrochemical desorption (Heyrovsky step). The value of the Tafel slope can qualitatively reveal the rate-determining step (RDS) of the HER mechanism. If the Volmer step is RDS, the observed Tafel slope value should be 120 mV dec⁻¹, and if the Heyrovsky or Tafel step is RDS,

the slope value is 40 or 30 mV dec⁻¹, respectively. The obtained Tafel slope of 88 mV dec⁻¹ for Au1Pt8 catalyst suggests the Volmer-Heyrovsky route (value of Tafel slope between 120 and 40 mV dec⁻¹) is the operative mechanism with the Heyrovsky (electrochemical desorption) step is RDS in the Au1Pt8-electrocatalyzed HER. To further assess and understand the intrinsic specific activity of the as-synthesized catalysts, surface-active sites, TOF, and mass activity were also investigated. The accessible number of active sites (n) was quantified according to the equation ($n = Q_s/F$) from the CV curves of as-synthesized electrocatalysts obtained in the potential window from -0.075–0.65 V vs RHE at 50 mV s⁻¹ in 1.0-M KOH (Fig. S5). The calculated values of n show that the Au1Pt8 electrocatalyst has more accessible active sites of $6.362 \cdot 10^{-7}$ mol cm⁻² than Au1Pt4 ($4.520 \cdot 10^{-7}$), Au1Pt1 ($3.293 \cdot 10^{-7}$), Au4Pt1 ($1.825 \cdot 10^{-7}$), and Au8Pt1 ($1.542 \cdot 10^{-7}$), which leads to improved HER activity. The estimated TOF and mass activity for the synthesized AuPt catalysts over a wide potential range of HER are displayed in Fig. S6(a and b). Among the investigated catalysts, Au1Pt8 catalyst has significantly higher TOF and mass activity at all measured H_2 evolution potentials (Fig. 4d and e). The calculated TOF for Au1Pt8 is 0.00442 s^{-1} at $\eta = 0.20 \text{ V}$, which is 2.2, 2.1, 9.1, and 13.6 times higher than that for Au1Pt4 (0.00199 s^{-1}), Au1Pt1 (0.00205 s^{-1}), Au4Pt1 (0.000487 s^{-1}), and Au8Pt1 (0.0003238 s^{-1}), respectively (Fig. 4d).

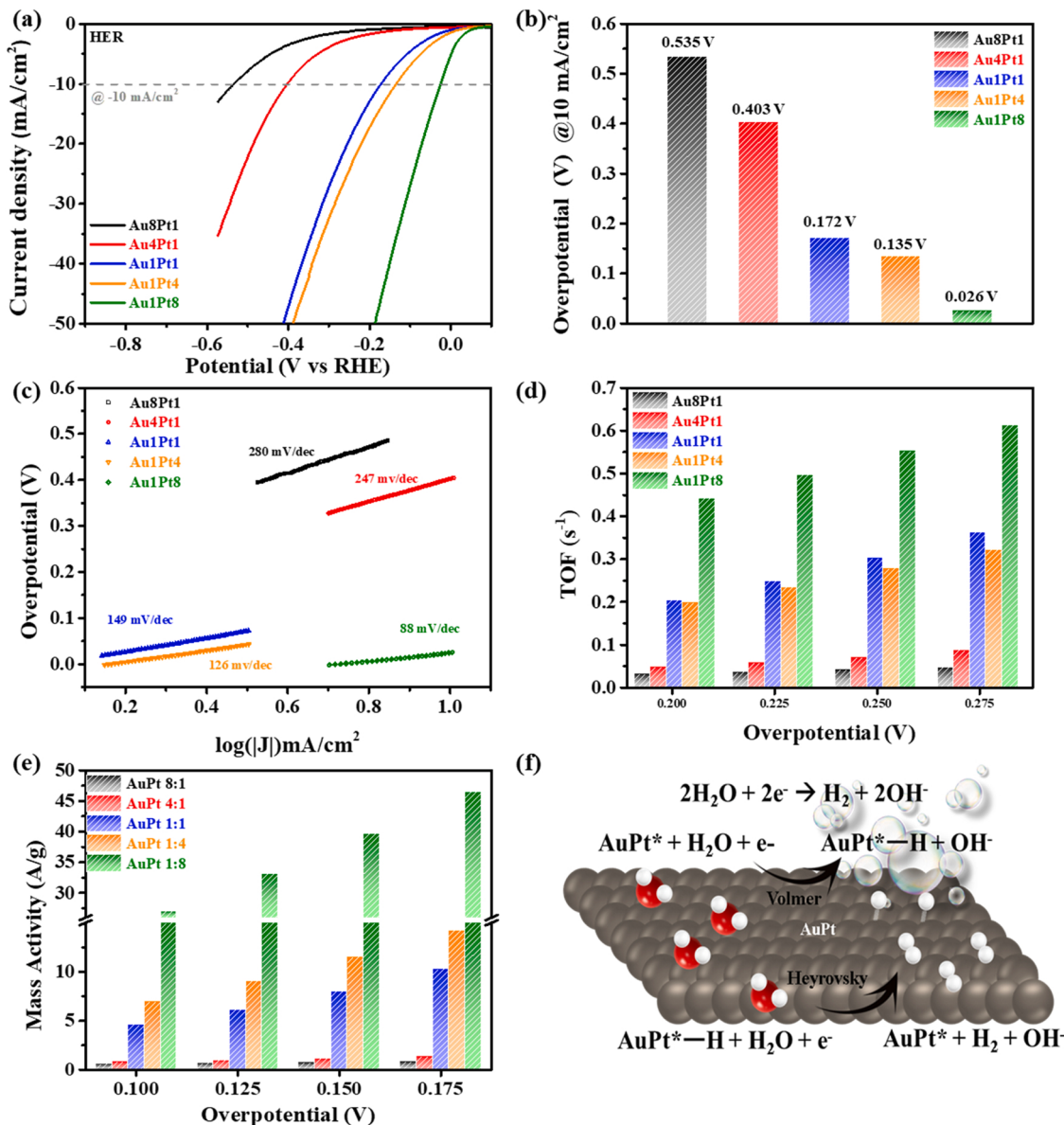


Fig. 4. HER performance of the synthesized various compositions of AuPt alloys: (a) LSV polarization curves, (b) summarized overpotential to deliver 10 mA cm^{-2} , (c) Tafel plot, (d and e) TOF and mass activity obtained at different overpotentials, and (f) reaction mechanism involved during HER.

Simultaneously, Au1Pt8 shows the highest mass activity of 46.54 A g^{-1} at $\eta = 0.175 \text{ V}$ (Fig. 4e). The observed results indicate that the Au1Pt8 composition can significantly improve the intrinsic activity and thus provide notable HER performance. On the basis of the HER results, the mechanism involved in the reaction is schematically illustrated in Fig. 4f. Furthermore, the amount of H_2 produced during 30 min of bulk electrolysis in 1.0 M KOH at -1.15 V vs Hg/HgO was quantified using GC (Fig. S7 a and b). The amount of H_2 shows a linear relationship with the electrolysis time (Fig. S8). The production rate is measured to be about $336 \mu\text{mol} / \text{h}$, demonstrating its potential as an effective electrocatalyst for commercial applications in renewable H_2 fuel production.

Further, to give a better sight of the enhanced catalytic activity of Au1Pt8 nanoalloys from the atomic point of view, we performed DFT calculations for a representative structure of the Au1Pt8 alloy (Fig. S9a), using the GPAW code [47] with the PBE functional [48] and an energy cut-off of 400 eV for the plane waves. The calculated lattice parameter agrees well with the result reported in Table S1, with a distance between neighboring atoms of 2.76 \AA , showing a slight decrease in the lattice parameter. The projected density of state (DOS) onto the Au and Pt

metals d-bands is depicted in Fig. S9b. The DOS diagram shows a significant overlap of the d-band of both Au and Pt metals. Furthermore, it is evident that after alloying, the Pt d band still spans the Fermi level, which is an essential characteristic of a promising electrocatalyst.

3.3. Electrocatalytic HzOR

The electrocatalytic activity of the AuPt alloys of different compositions concerning HzOR was evaluated in a solution comprising $0.5\text{-M N}_2\text{H}_4$ in 1.0-M KOH using a conventional three-electrode arrangement. The obtained anodic polarization curves measured at 5 mV s^{-1} are shown in Fig. 5a. The Au1Pt8 alloy exhibits a substantially boosted HzOR activity requiring a low overpotential of 0.483 and 0.502 V to attain 5 and 10 mA cm^{-2} , respectively. For comparison, Au8Pt1 shows practically poor HzOR activity requiring an η of 0.715 V to deliver 10 mA cm^{-2} (Fig. 5b), which indicates the possibility to remarkably enhance HzOR activity by building an optimized composition of Au and Pt in AuPt alloy. The corresponding Tafel slope of Au1Pt8 is 60 mV dec^{-1} , which is lower than that of Au1Pt4 (71 mV dec^{-1}), Au1Pt1

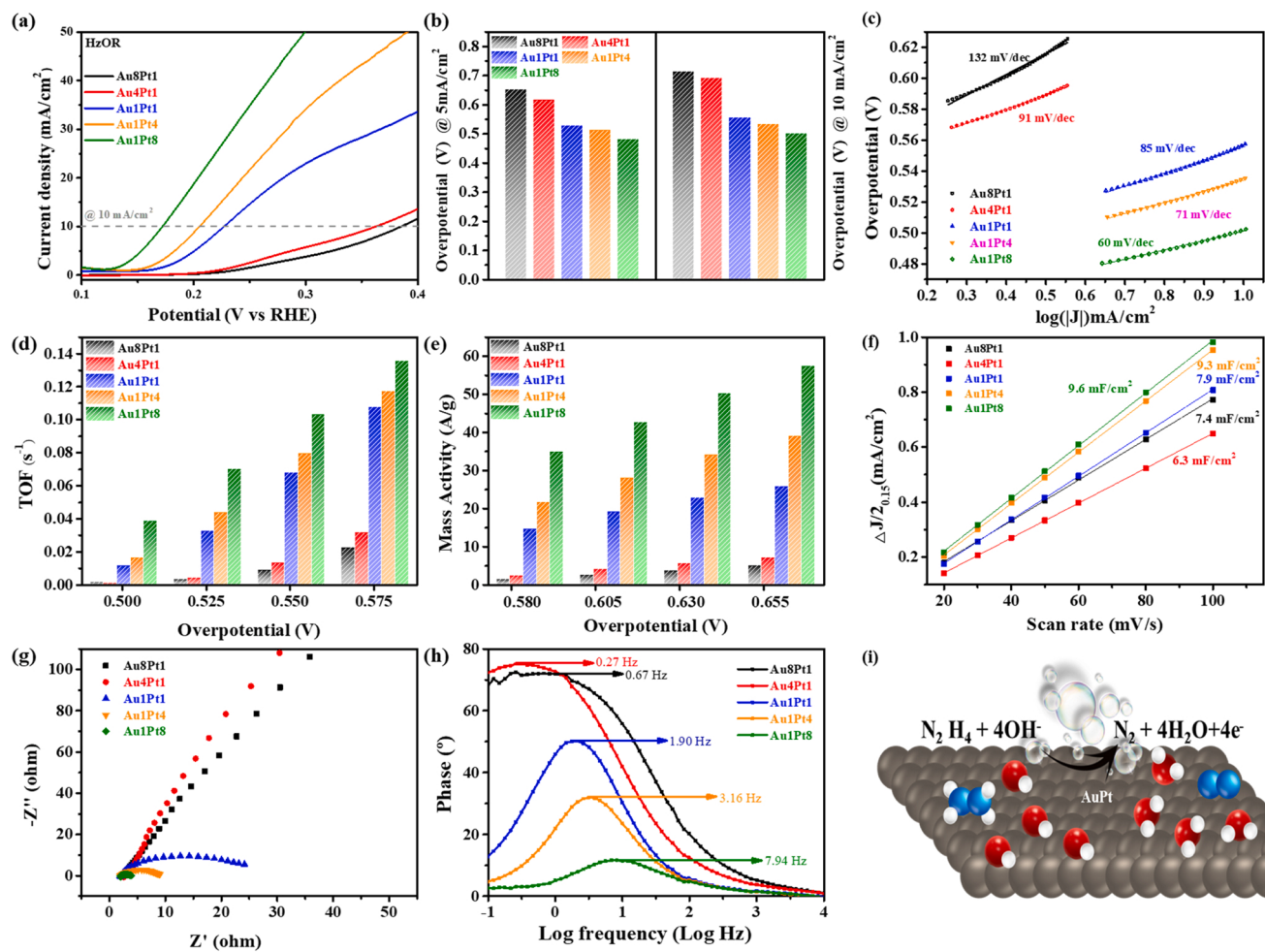


Fig. 5. HzOR performance of the synthesized various compositions of AuPt alloys: (a) LSV anodic polarization curves, (b) summarized overpotential to deliver 5 and 10 mA cm^{-2} , (c) Tafel plot, (d and e) TOF and mass activity obtained at different overpotentials, (f) $\Delta J/J_015$ vs scan rate plots for the estimation of C_{dl} , (g and h) Nyquist and Bode plots measured at a constant potential of -0.75 V vs Hg/HgO, and (i) reaction mechanism involved during HzOR.

(85 mV dec^{-1}), Au4Pt1 (91 mV dec^{-1}), and Au8Pt1 (132 mV dec^{-1}), which signifies the faster HzOR kinetics of Au1Pt8 alloy as well as HER (Fig. 5c). An exceptional catalytic property of Au1Pt8 can be attributed to its chemical structure. During the formation of AuPt nanoalloy, the d-charge depletion was observed in Pt due to its electropositive nature, which is later neutralized by the electron redistribution process resulting in an empty 6 s orbital. Thus, the formed empty 6 s orbitals play a key role in the chemisorption of N_2H_4 onto the catalytic surface, forming a dative bond between two lone pairs of electrons of nitrogen atoms in N_2H_4 and empty 6 s orbitals of Pt. This facilitates the decomposition of the N–H bond in N_2H_4 by strongly retaining the N–N bond on the catalyst surface, resulting in the desorption of N_2 , as shown in Scheme S1 [49]. Particularly, the remarkable enhancement in HzOR activity creates Au1Pt8 rival the performance of the recently reported catalyst (Table S5). Further, the TOF per surface site of the synthesized nanoalloy electrocatalysts was estimated to assess the intrinsic nanocatalytic activities toward HzOR (Figs. S10a and 5d). The estimated TOF value of Au1Pt8 is 0.103 s^{-1} at $\eta = 0.55 \text{ V}$, which is higher than that of Au1Pt4 (0.079 s^{-1}), Au1Pt1 (0.068 s^{-1}), Au4Pt1 (0.013 s^{-1}), and Au8Pt1 (0.009 s^{-1}), as displayed in Fig. 5d. Similarly, the mass activity of the Au1Pt8 is significantly higher compared with that of other compositions of AuPt alloy at the measured potentials, as shown in Figs. S10b and 5e. Thus, the mass activity trend and estimated TOF values are fully consistent with the intrinsic electrocatalytic activity for HzOR, demonstrating that increased Au1Pt8 activity mainly benefits from the positive synergistic effects caused by the intrinsic electron effect in terms of the

electron redistribution in AuPt alloy. To better understand the exceptional high HzOR activity of Au1Pt8 and, more importantly, its distinct advantages over other AuPt alloy compositions, we assessed C_{dl} from the CV curves obtained in the non-Faradaic region (Fig. S11) to estimate the ECSA, which is the value directly proportional to the catalytically active sites [27]. As expected, the estimated C_{dl} values of the AuPt alloys are in well accordance with the trend of HzOR performances, i.e., Au1Pt8 (9.6 mF cm^{-2}) $>$ Au1Pt4 (9.3 mF cm^{-2}) $>$ Au1Pt1 (7.9 mF cm^{-2}) $>$ Au4Pt1 (7.4 mF cm^{-2}) $>$ Au8Pt1 (6.3 mF cm^{-2}), as shown in Fig. 5f. Among the various compositions of AuPt alloys, Au1Pt8 (0.109 mF cm^{-2}) has the highest ECSA value, compared with Au1Pt4 (0.105 mF cm^{-2}), Au1Pt1 (0.089 mF cm^{-2}), Au4Pt1 (0.084 mF cm^{-2}), and Au8Pt1 (0.071 mF cm^{-2}). These changes in ECSA values are related to the composition of AuPt alloys. EIS analyses were performed to further explore the electrode kinetics during the HzOR process (Fig. 5g). The calculated impedance parameters using ZSim software are given in Table S6, indicating the much smaller charge transfer resistance (R_{ct}) values of the Au1Pt8 catalyst, which is in the order of Au1Pt8 (1.58Ω) $<$ Au1Pt4 (6.26Ω) $<$ Au1Pt1 (20.03Ω) $<$ Au4Pt1 (346.99Ω) $<$ Au8Pt1 (392.62Ω). The Nyquist plots of EIS measurements (Fig. 5g) show that the optimal composition of the Au1Pt8 alloy provided faster charge transfer with good electrical conductivity and more favorable electrode kinetics for HzOR catalysis [50,51]. Bode plots were also derived to measure the lifetime of the electron (τ_e) from the frequency peak (f_{max}) at a fixed potential of -0.75 V vs Hg/HgO, as depicted in Fig. 5h. The lifetime of the electron can be assessed according to relation, τ_e

$= 1/(2\pi f_{\max})$ and the estimated τ_e values for Au1Pt8, Au1Pt4, Au1Pt1, Au4Pt1, and Au8Pt1 are 12.46, 4.96, 2.98, 0.42, and 1.05 s, respectively (Table S6). The Au1Pt8 exposed a lower relaxation time compared with the other compositions of AuPt alloys, suggesting the high HzOR activity. The schematic view of the possible reaction mechanism involved during HzOR is illustrated in Fig. 5i.

The FT-IR analysis was carried out for the recovered catalyst of optimal Au1Pt8 nanoalloys with carbon support from the optimized experimental conditions in order to ascertain the surface chemisorption/adsorption of hydrazine on the catalyst during mechanistic pathway. After the LSV experiment towards HzOR, the Au1Pt8 catalyst was separated from the solution, air dried, and used for FT-IR analysis, as displayed in Fig. S12. The spectrum of pure hydrazine reveals the characteristic peaks of the NH_2 group at $3,300 \text{ cm}^{-1}$ and $1,630 \text{ cm}^{-1}$, which can be ascribed to the asymmetric stretching vibration of the N-H

group and H-N-H bending vibrations, respectively [52]. In the meantime, the recovered catalyst exhibits peak splitting with a large downshift in the spectra, which could be due to the weakening of N-H bond in hydrazine after coordinating to Au1Pt8 as a bridged bidentate ligand (as shown in Scheme S1 of the mechanistic reaction pathway). This behavior is further confirmed by the appearance of new peak for the N-N stretching frequency at 878 cm^{-1} , typical for a bidentate bridging nature of hydrazine molecules [53]. Further, the specific surface area and porosity of the optimal Au1Pt8 nanoalloy with carbon support were investigated using BET-nitrogen adsorption and desorption isotherm analysis (Fig. S12). The obtained nitrogen adsorption and desorption isotherm exhibit type IV with H_2 hysteresis loop (Fig. S13 a), and the existence of cylindrical-shaped hysteresis suggests the mesoporous nature [54]. The specific surface area and pore volume of the optimal Au1Pt8 nanoalloy with carbon support were found to be $\sim 293.3 \text{ m}^2 \text{ g}^{-1}$

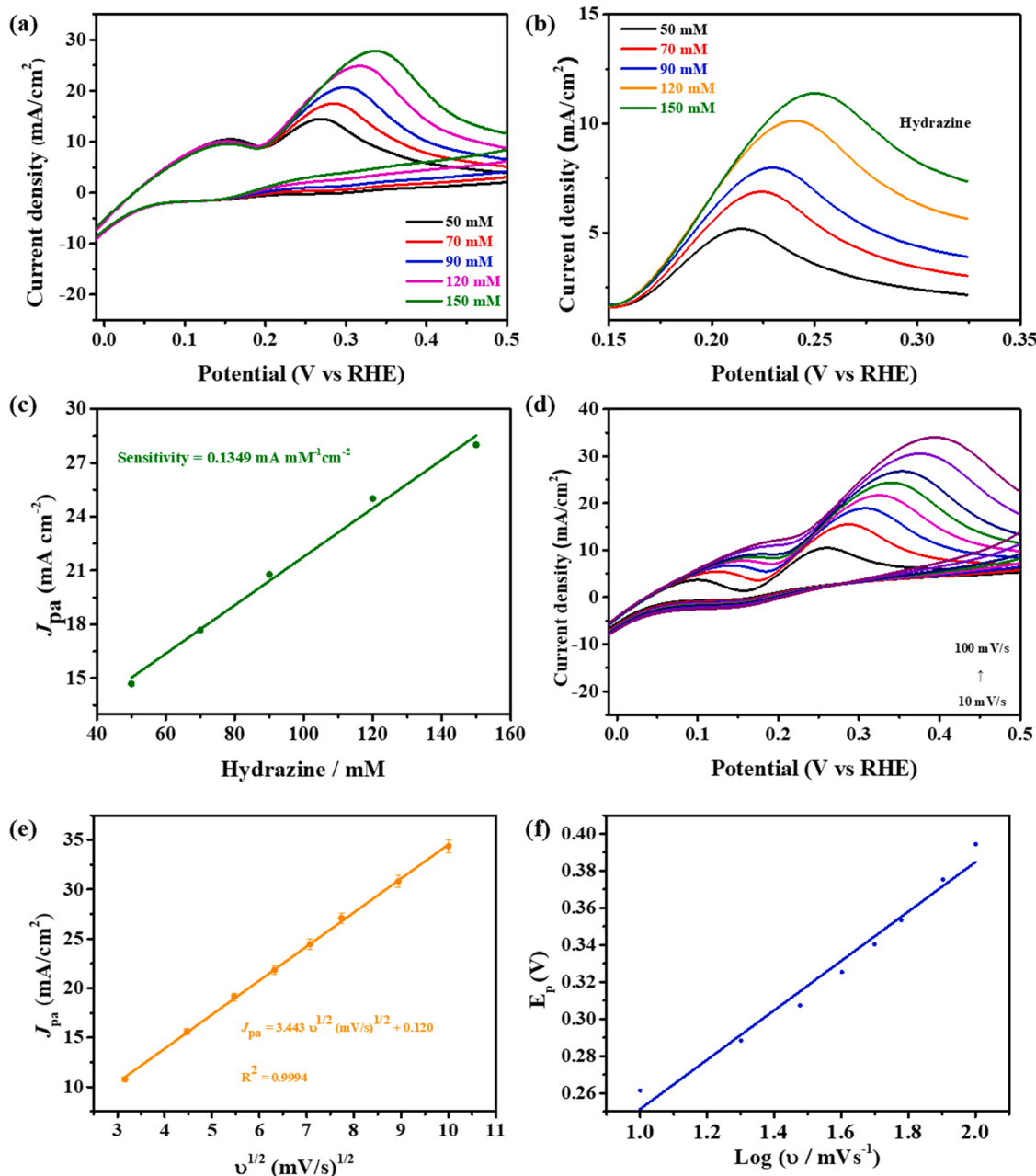


Fig. 6. (a and b) CV and LSV profiles for the HzOR activity of optimal Au1Pt8 nanoalloy at various N_2H_4 concentrations in the range of 50–150 mM in 1.0-M KOH, (c) N_2H_4 concentration vs anodic oxidation peak current density (J_{pa}) linear plot, (d) CV curves at diverse scan rates in 150 mM of N_2H_4 in 1.0-M KOH, (e) linear plot of J_{pa} vs $v^{1/2}$, and (f) E_p vs $\log(v)$.

and $1.207 \text{ cm}^3 \text{ g}^{-1}$, respectively (Fig. S13a and b). The large specific surface area, porous structure, and electron redistribution make Au1Pt8 a promising electrocatalyst by providing better surface adsorption properties.

We then studied the effect of N_2H_4 concentration and scan rate on the voltammetric waves to get insight into the electrocatalytic HzOR mechanism on Au1Pt8. The anodic peak current increases with concentrations ranging from 50 to 150 mM (Fig. 6a and b), indicating that Au1Pt8 is effective for electrocatalyzing the HzOR and extremely sensitive to N_2H_4 ($0.134 \text{ mA mM}^{-1} \text{ cm}^{-2}$) (Fig. 6c). By changing the scan rates (v) of CV (Fig. 6d), the resulting oxidation peak current density (J_{pa}) and peak potential (E_p) vary linearly with $v^{1/2}$ and $\log(v)$, respectively (Fig. 6e and f), indicating the HzOR over Au1Pt8 is a diffusion-controlled and irreversible process [55,56].

3.4. Electrocatalytic OER

The aforementioned HER and HzOR prove the excellent electrocatalytic activity of the Au1Pt8 catalyst. We have also evaluated and compared the electrochemical performance of various compositions of AuPt alloys toward OER in a 1.0-M KOH electrolyte. The obtained LSV curves during OER tests for Au1Pt8, Au1Pt4, Au1Pt1, Au4Pt1, and Au8Pt1 are shown in Fig. 7a. In addition, the catalytic performance of AuPt alloys with different compositions was evaluated using overpotential (η) to deliver current densities 5 and 10 mA cm^{-2} (Fig. 7b). The η was obtained at the point of current density, based on the relation $\eta = (E_{RHE} - 1.23 \text{ V})$, where E_{RHE} is the measured potential against RHE and 1.23 V is the theoretical water oxidation potential against RHE. From Fig. 7b, it is evident that the Au1Pt4 exhibits a high OER activity with a low η of 0.437 V to deliver 5 mA cm^{-2} and 0.473 V to deliver 10 mA cm^{-2} , which confers the best electrocatalytic OER performance among other AuPt alloys, whereas the Au1Pt8, Au1Pt1, Au4Pt1, and

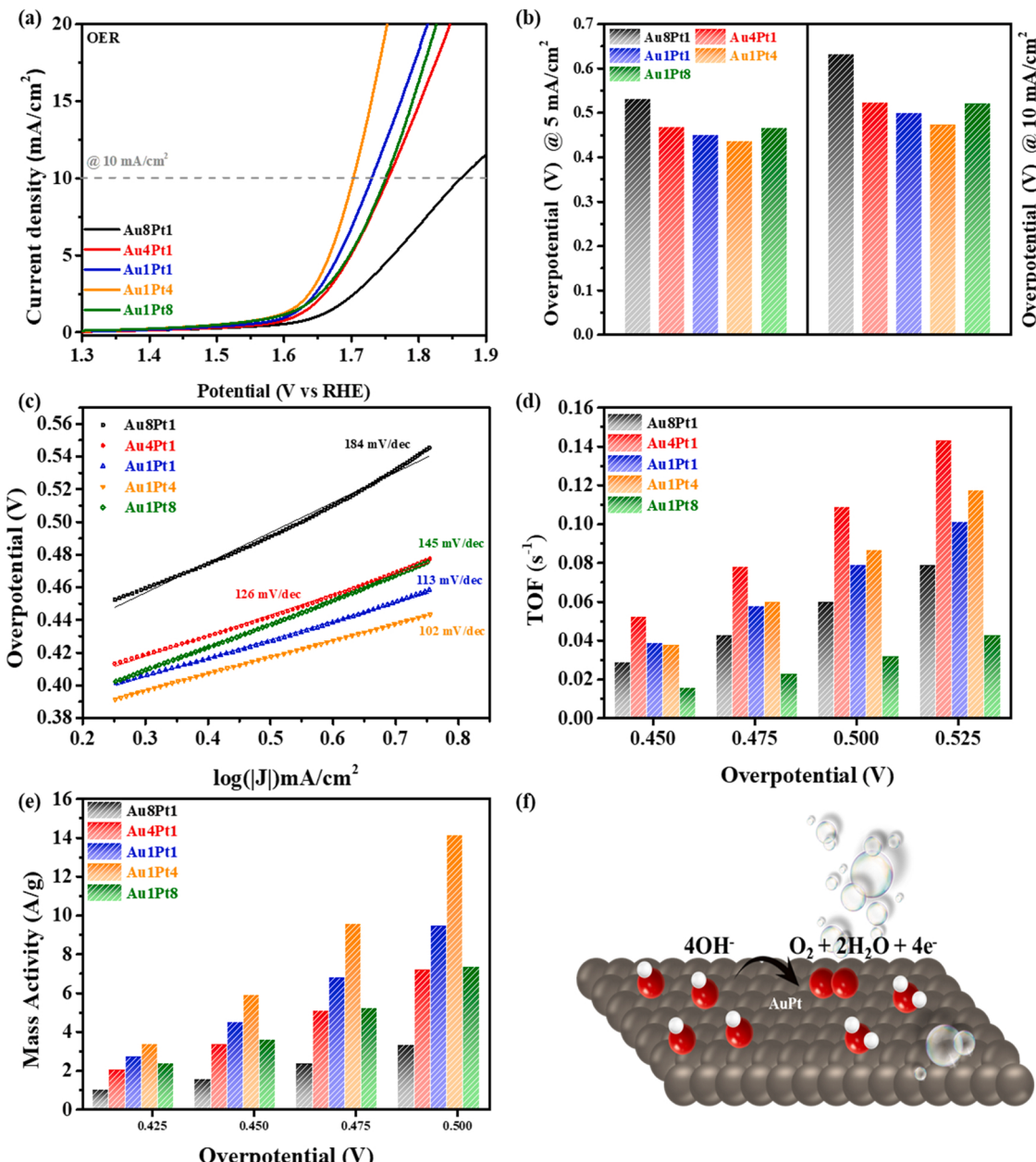
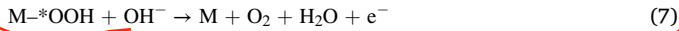
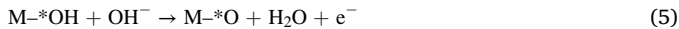


Fig. 7. OER performance of the synthesized AuPt alloys with various compositions: (a) LSV polarization curves, (b) summarized overpotential to deliver 5 and 10 mA cm^{-2} , (c) Tafel plot, (d and e) TOF and mass activity obtained at different overpotentials, and (f) reaction mechanism involved during OER.

Au8Pt1 require high η of 0.467 (0.521), 0.451 (0.500), 0.469 (0.524), and 0.532 (0.633) V, respectively, to deliver 5 mA cm^{-2} (10 mA cm^{-2}). Moreover, the derived Tafel plots from the LSV curves are depicted in Fig. 7c. The Tafel slope of Au1Pt4 for OER is 102 mV dec^{-1} , which is lower than that of Au1Pt8 (145 mV dec^{-1}), Au1Pt1 (113 mV dec^{-1}), Au4Pt1 (126 mV dec^{-1}), and Au8Pt1 (184 mV dec^{-1}), signifying that Au1Pt4 has the best OER kinetics among all other compositions of AuPt alloys. However, the pure noble metals of Au and Pt are almost inactive or show a high η in the OER [57,58]. For comparison, the OER activity of pure Au and Pt metal nanoparticles was examined and the resulting LSV curves show the highest η values, which revealed the lowest OER activity compared to AuPt alloy (Fig. S14). Thus, the obtained results are in good correlation with the previous studies on the OER activity series of noble metals with Ru > Ir > Rh > Pd > Pt > Au [59,60]. For instance, the lower OER activity of pure Pt metal is due to the formation of poorly conductive Pt oxides species during the OER potential range which covered the surface of active sites. During the OER process, the electrons should tunnel via this oxide layer where the performance is mainly reliant on the thickness of the oxide layer. However, the growth of species is faster due to the high noticeable oxophilicity nature of Pt and the poorly conductive oxide layer becomes thicker on the surface of Pt metal nanoparticles, which decreases the OER current and lower OER activity [61]. Highlighted by the concept of developing a multifunctional electrocatalyst, the advantages of alloying Pt and Au improve the OER activity. As we have seen, the Pt-rich composition of Au1Pt8 possesses an excellent HER and HzOR activity, whereas Au1Pt8 shows lower OER activity. In general, the electrode materials can undergo surface oxidation at high applied potential, so the electrode surface no longer consists of a pure metal electrocatalyst. Thus, the low OER activity of Au1Pt8 might be due to the surface oxidation of electrode material at higher potentials and forms poorly conducting PtO, resulting in high η in the OER [58,62]. Based on previous reports, the water oxidation (OER) reaction under alkaline media involves the following reaction mechanism:



The reaction above is mostly expected to proceed in four fundamental steps (Eqs. (4)–(7)):



where M signifies the active surface site of the catalyst and M- $^*\text{OH}$, M- $^*\text{O}$, and M- $^*\text{OOH}$ refer to the intermediate species ($^*\text{OH}$, $^*\text{O}$, and $^*\text{OOH}$, respectively) adsorbed on the active surface sites of the electrocatalyst [63]. Initially, the M- $^*\text{OH}$ formation occurs through the one-electron oxidation of adsorbed hydroxide anions on the active surface site of the catalyst (Eq. 4). Followed by the transformation of M- $^*\text{OH}$ into M- $^*\text{O}$ with the removal of a couple of electrons and protons (Eq. 5). Then, M- $^*\text{O}$ combines with OH $^-$ and transfers to M- $^*\text{OOH}$ via one-electron oxidation (Eq. 6). Consequently, one more proton-coupled electron transfer reaction continues, generating the O₂ gas and the initial active surface site of the catalyst (Eq. 7). All the intermediates of the OER reaction are bound to the catalyst surface as oxo or peroxy compounds. The OER catalytic surface intermediates and their properties mainly depend on the nature of the catalyst materials, and reaction conditions used [64]. Also, the XPS evidence of the Pt²⁺ occurring on the surface of AuPt alloys during the charge neutrality process (Fig. 3f) directly reinforces the participation of Pt⁰ at the AuPt alloy providing the 1 and/or 2 electrons involved in the OER mechanism, strongly supporting our OER mechanism proposition. Further, the TOF represents the direct comparison of intrinsic activities of the catalysts for OER

(Figs. S15a and 7d). The estimated TOF values reveal that Au1Pt4 has the highest TOF value of 0.086 s^{-1} at $\eta = 0.50 \text{ V}$ compared with other electrocatalysts: Au1Pt8 (0.031 s^{-1}), Au1Pt1 (0.078 s^{-1}), Au4Pt1 (0.109 s^{-1}), and Au8Pt1 (0.059 s^{-1}). Thus, the enhanced OER activity may be due to the highly accessible active surface sites in Au1Pt4. The OER activity of the various compositions of AuPt alloys per gram of sample is shown in Figs. S15b and 7e. As a result, the attained mass activity of Au1Pt4 is 14.15 A g^{-1} at $\eta = 0.50 \text{ V}$, which is higher compared with that of other compositions of AuPt alloys.

3.5. Overall hydrazine and water splitting performance

Considering the best bifunctional electrocatalytic activity of Au1Pt8 for both HER and HzOR, we constructed a two-electrode OH_S electrolyzer using Au1Pt8/CC as both anode and cathode with 0.5-M N₂H₄ in 1.0-M KOH electrolyte. For comparison, OWS was also performed using the similar two-electrode Au1Pt8/CC || Au1Pt8/CC system without the addition of N₂H₄ (Fig. 8a). Upon cell performance, massive gas bubbles were evolved at the surface of Au1Pt8/CC electrode on both cathode and anode parts, indicating the simultaneous existence of HER (H₂ evolution) and HzOR (N₂ evolution) for OH_S; whereas HER (H₂ evolution) and OER (O₂ evolution) for OWS (Fig. 8b and c and video SV1 for H₂ and N₂ evolution during OH_S). As depicted in Fig. 8a, the Au1Pt8/CC || Au1Pt8/CC hybrid electrolyzer for OH_S requires cell voltages of 0.172 and 0.427 V to achieve 10 and 50 mA cm^{-2} , respectively. In contrast, the OWS electrolyzer has achieved the same current density at much higher voltages of 1.773 and 2.136 V in the absence of N₂H₄, indicating the advantage of replacing OER with HzOR in the anode part which is relatively high conducive to energy-saving electrolyzer for H₂ production. More importantly, we studied the long-term durability of Au1Pt8/CC || Au1Pt8/CC hybrid electrolyzer in OH_S with continuous electrolysis for 10 h for practical applications (Fig. 8d). As a result, Au1Pt8/CC || Au1Pt8/CC electrolyzer showed good durability in the separation of HER and HzOR with a very slight increase in cell potential. Remembering the structural retention properties, we continued with surface morphological analysis using FE-SEM after long-term electrolysis, as shown in the inset of Fig. 8d. Noticeably, the Au1Pt8/CC electrode could retain the overall initial surface structure even after long-term electrolysis. For comparison, we also provided the FE-SEM image of pure CC in the inset of Fig. 8d. Remarkably, the performance of OH_S using Au1Pt8/CC || Au1Pt8/CC electrolyzer is comparable, if not superior, with that of recently reported literature on bifunctional HER and HzOR catalysts (Table S7).

4. Conclusions

The various AuPt alloy compositions were synthesized using a simple integrated PLI and ultrasonochemical process as robust multifunctional (HER, HzOR, and OER) electrocatalysts in an alkaline medium. The AuPt alloy has high chemisorption activity of N₂H₄ due to the formation of a dative bond among the lone pair electrons of two N-atoms of N₂H₄ and the empty 6 s orbitals of Pt in AuPt alloy, indicating its high intrinsic activity against HzOR. The Au1Pt8 has more accessible ECSA, resulting in abundant surface-active sites that contribute to enhanced HER and HzOR activity. The direct mixing of carbon black with AuPt alloy during the laser-assisted synthesis process constructs a well-dispersed AuPt alloy network and provides the electrocatalysts with good electrical conductivity. In particular, the Au1Pt8 alloy exhibits an ultralow η of 26 mV at 10 mA cm^{-2} with a small Tafel slope of 88 mV dec^{-1} for HER in an alkaline medium. For HzOR, the Au1Pt8 electrode requires an η of 502 mV to attain 10 mA cm^{-2} with Tafel slope of 60 mV dec^{-1} in 0.5-M N₂H₄/1.0-M KOH electrolyte. Impressively, the designed two-electrode (Au1Pt8/CC || Au1Pt8/CC) hybrid electrolyzer for OH_S using the Au1Pt8 alloy as a bifunctional (HER and HzOR) electrocatalyst can deliver 10 and 50 mA cm^{-2} current densities at a much lower cell voltage of ~ 0.172 and 0.427 V , which significantly outperforms the

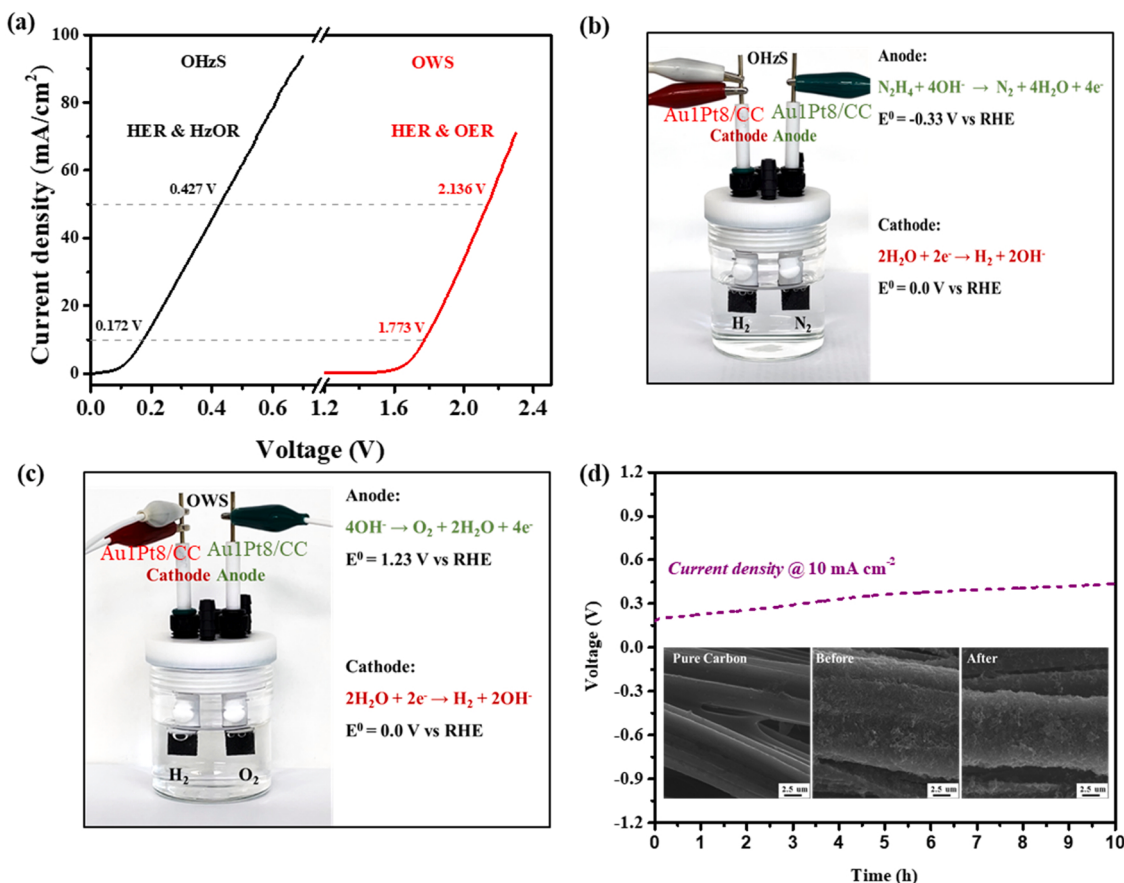


Fig. 8. (a) Comparison of the cell voltages from LSV curves of OHzS and OWS for the optimized Au1Pt8 alloy in a two-electrode (Au1Pt8/CC || Au1Pt8/CC) electrolyzer with a scan rate of 5 mV s⁻¹, (b and c) optical image of the OHzS and OWS electrolyzer system, and (d) long-term durability of Au1Pt8/CC || Au1Pt8/CC hybrid electrolyzer in OHzS with continuous electrolysis over 10 h at 10 mA cm⁻². The insets in (d) show the FE-SEM surface structure of pure CC, Au1Pt8/CC before and after electrolysis.

OWS electrolyzer requiring ~1.773 and 2.136 V, respectively. This study demonstrates that optimizing the various Au and Pt composition ratios could efficiently modulate the electronic structure of the AuPt alloys, increasing the feasibility of AuPt alloys for hydrazine fuel cells to consistently achieve both electrical energy and high-rate H₂ fuel generation.

CRediT authorship contribution statement

Yiseul Yu: Conceptualization, Investigation, Writing – original draft. **Seung Jun Lee:** Data curation, Methodology, Investigation, Visualization. **Jayaraman Theerthagiri:** Data curation, Conceptualization, Methodology, Investigation, Visualization. **Yeryeong Lee:** Data curation, Writing – review & editing. **Myong Yong Choi:** Supervision, Writing – review & editing, Funding acquisition.

Declaration of Competing Interest

The authors declare that they have no known competing financial interests or personal relationships that could have appeared to influence the work reported in this paper.

Acknowledgements

This research was supported by Korea Basic Science Institute (National research Facilities and Equipment Center) grant funded by the Ministry of Education. (No. 2019R1A6C1010042, 2021R1A6C103A427). The authors, Prof. M. Y. Choi, Dr. J. Theerthagiri, and Dr. S. J. Lee, acknowledge

the financial support from National Research Foundation of Korea (NRF), (2022R1A2C2010686, 2019H1D3A1A01071209, 2020R1I1A1A01065748, 2021R1I1A1A01060380). The authors also like to acknowledge Dr. Prof. Leandro M.C. Pinto, Universidade Federal de Mato Grosso do Sul, UFMS, Brazil for his help of the DFT calculations.

Appendix A. Supporting information

Supplementary data associated with this article can be found in the online version at doi:10.1016/j.apcatb.2022.121603.

References

- [1] Q. Qian, J. Zhang, J. Li, Y. Li, X. Jin, Y. Zhu, Y. Liu, Z. Li, A. El-Harairy, C. Xiao, G. Zhang, Y. Xie, Artificial heterointerfaces achieve delicate reaction kinetics towards hydrogen evolution and hydrazine oxidation catalysis, *Angew. Chem. Int. Ed.* 60 (2021) 5984–5993.
- [2] J. Theerthagiri, E.S.F. Cardoso, G.V. Fortunato, G.A. Casagrande, B. Senthilkumar, J. Madhavan, G. Maia, Highly electroactive Ni pyrophosphate/Pt catalyst toward hydrogen evolution reaction, *ACS Appl. Mater. Interfaces* 11 (2019) 4969–4982.
- [3] J. Theerthagiri, S.J. Lee, A.P. Murthy, J. Madhavan, M.Y. Choi, Fundamental aspects and recent advances in transition metal nitrides as electrocatalysts for hydrogen evolution reaction: a review, *Curr. Opin. Solid State Mater. Sci.* 24 (2020), 100805.
- [4] L. Guo, Q. Liu, Y. Liu, Z. Chen, Y. Jiang, H. Jin, T. Zhou, J. Yang, Y. Liu, Self-supported tremella-like MoS₂-AB particles on nickel foam as bifunctional electrocatalysts for overall water splitting, *Nano Energy* 92 (2022), 106707.
- [5] H.-Y. Sun, G.-R. Xu, F.-M. Li, Q.-L. Hong, P.-J. Jin, P. Chen, Y. Chen, Hydrogen generation from ammonia electrolysis on bifunctional platinum nanocubes electrocatalysts, *J. Energy Chem.* 47 (2020) 234–240.
- [6] Y. Ding, K.-W. Cao, J.-W. He, F.-M. Li, H. Huang, P. Chen, Y. Chen, Nitrogen-doped graphene aerogel-supported ruthenium nanocrystals for pH-universal hydrogen evolution reaction, *Chin. J. Catal.* 43 (2022) 1535–1543.

- [7] J. Bai, N. Jia, P. Jin, P. Chen, J.-X. Jiang, J.-H. Zeng, Y. Chen, Metal-organic interface engineering for boosting the electroactivity of Pt nanodendrites for hydrogen production, *J. Energy Chem.* 51 (2020) 105–112.
- [8] M. Zhang, H. Li, P. Cai, K. Chen, Z. Wen, High-performance flow alkali-Al/acid hybrid fuel cell for high-rate H₂ generation, *Adv. Funct. Mater.* 31 (2021), 2103248.
- [9] G. Wang, J. Chen, P. Cai, J. Jia, Z. Wen, A self-supported Ni–Co perselenide nanorod array as a high-activity bifunctional electrode for a hydrogen-producing hydrazine fuel cell, *J. Mater. Chem. A* 6 (2018) 17763–17770.
- [10] H. Fu, Y. Wang, Y. Jiao, G. Yang, H. Yan, C. Tian, A. Wu, Y. Liu, Vanadium-incorporated CoP₂ with lattice expansion for highly efficient acidic overall water splitting, *Angewandte Chemie International Edition* 134 (2022), e202116233.
- [11] S. Ramakrishnan, D.B. Velusamy, S. Sengodan, G. Nagaraju, D.H. Kim, A.R. Kim, D. J. Yoo, Rational design of multifunctional electrocatalyst: an approach towards efficient overall water splitting and rechargeable flexible solid-state zinc-air battery, *Appl. Catal. B: Environ.* 300 (2022), 120752.
- [12] S.J. Lee, J. Theerthagiri, P. Nithyadarseni, P. Arunachalam, D. Balaji, A. Madan Kumar, J. Madhavan, V. Mittal, M.Y. Choi, Heteroatom-doped graphene-based materials for sustainable energy applications: a review, *Renew. Sustain. Energy Rev.* 143 (2021), 110849.
- [13] P. Li, G. Zhao, P. Cui, N. Cheng, M. Lao, X. Xu, S.X. Dou, W. Sun, Nickel single atom-decorated carbon nanosheets as multifunctional electrocatalyst supports toward efficient alkaline hydrogen evolution, *Nano Energy* 83 (2021), 105850.
- [14] Y. Zhao, N. Jia, X.-R. Wu, F.-M. Li, P. Chen, P.-J. Jin, S. Yin, Y. Chen, Rhodium phosphide ultrathin nanosheets for hydrazine oxidation boosted electrochemical water splitting, *Appl. Catal. B: Environ.* 270 (2020), 118880.
- [15] Y. Li, Y. Zhao, F.-M. Li, Z. Dang, P. Gao, Ultrathin NiSe nanosheets on Ni foam for efficient and durable hydrazine-assisted electrolytic hydrogen production, *ACS Appl. Mater. Interfaces* 13 (2021) 34457–34467.
- [16] Y. Yan, J.-Y. Zhang, X.-R. Shi, Y. Zhu, C. Xia, S. Zaman, X. Hu, X. Wang, B.Y. Xia, A zeolitic-imidazole framework-derived trifunctional electrocatalyst for hydrazine fuel cells, *ACS Nano* 15 (2021) 10286–10295.
- [17] Y. Li, J. Zhang, Y. Liu, Q. Qian, Z. Li, Y. Zhu, G. Zhang, Partially exposed RuP₂ surface in hybrid structure endows its bifunctionality for hydrazine oxidation and hydrogen evolution catalysis, *Sci. Adv.* 6 (2020) eabb4197.
- [18] Q. Sun, M. Zhou, Y. Shen, L. Wang, Y. Ma, Y. Li, X. Bo, Z. Wang, C. Zhao, Hierarchical nanoporous Ni(Cu) alloy anchored on amorphous NiFeP as efficient bifunctional electrocatalysts for hydrogen evolution and hydrazine oxidation, *J. Catal.* 373 (2019) 180–189.
- [19] D. Khalafallah, M. Zhi, Z. Hong, Development trends on nickel-based electrocatalysts for direct hydrazine fuel cells, *ChemCatChem* 13 (2021) 81–110.
- [20] F. Liu, X. Jiang, H.-H. Wang, C. Chen, Y.-H. Yang, T. Sheng, Y.-S. Wei, X.-S. Zhao, L. Wei, Boosting electrocatalytic hydrazine oxidation reaction on high-index faceted Au concave trioctahedral nanocrystals, *ACS Sustainable Chemistry & Engineering*, (2022).
- [21] J. Yang, L. Xu, W. Zhu, M. Xie, F. Liao, T. Cheng, Z. Kang, M. Shao, Rh/RhO_x nanosheets as pH-universal bifunctional catalysts for hydrazine oxidation and hydrogen evolution reactions, *J. Mater. Chem. A* 10 (2022) 1891–1898.
- [22] J. Li, Y. Li, J. Wang, C. Zhang, H. Ma, C. Zhu, D. Fan, Z. Guo, M. Xu, Y. Wang, H. Ma, Elucidating the critical role of ruthenium single atom sites in water dissociation and dehydrogenation behaviors for robust hydrazine oxidation-boosted alkaline hydrogen evolution, *Adv. Funct. Mater.* 32 (2022), 2109439.
- [23] S. Varhade, Z.M. Bhat, R. Thimmappa, M.C. Devendrachari, A.R. Kottaiachamy, S. Khaire, S.P. Shafii, M.O. Thotiyil, An inherent heat driven fuel exhaling hydrazine fuel cell, *Chem. Phys. Lett.* 706 (2018) 553–557.
- [24] Y. Yu, J. Theerthagiri, S.J. Lee, G. Muthusamy, M. Ashokkumar, M.Y. Choi, Integrated technique of pulsed laser irradiation and sonochemical processes for the production of highly surface-active NiPd spheres, *Chem. Eng. J.* 411 (2021), 128486.
- [25] Q. Xue, X.-Y. Bai, Y. Zhao, Y.-N. Li, T.-J. Wang, H.-Y. Sun, F.-M. Li, P. Chen, P. Jin, S.-B. Yin, Y. Chen, Au core-PtAu alloy shell nanowires for formic acid electrolysis, *J. Energy Chem.* 65 (2022) 94–102.
- [26] L.D. Germano, V.S. Marangoni, N.V.V. Mogili, L. Seixas, C.M. Maroneze, Ultrasmall (<2 nm) Au@Pt nanostructures: Tuning the Surface electronic states for electrocatalysis, *ACS Appl. Mater. Interfaces* 11 (2019) 5661–5667.
- [27] Y. Yu, S. Jun Lee, J. Theerthagiri, S. Fonseca, L.M.C. Pinto, G. Maia, M. Yong, Choi, Reconciling of experimental and theoretical insights on the electroactive behavior of C/Ni nanoparticles with AuPt alloys for hydrogen evolution efficiency and non-enzymatic sensor, *Chem. Eng. J.* 435 (2022), 134790.
- [28] J. Liu, L. Cao, W. Huang, Z. Li, Preparation of AuPt alloy foam films and their superior electrocatalytic activity for the oxidation of formic acid, *ACS Appl. Mater. Interfaces* 3 (2011) 3552–3558.
- [29] J. Theerthagiri, A.P. Murthy, S.J. Lee, K. Karuppasamy, S.R. Arumugam, Y. Yu, M. M. Hanafiah, H.-S. Kim, V. Mittal, M.Y. Choi, Recent progress on synthetic strategies and applications of transition metal phosphides in energy storage and conversion, *Ceram. Int.* 47 (2021) 4404–4425.
- [30] S.J. Lee, J. Theerthagiri, M.Y. Choi, Time-resolved dynamics of laser-induced cavitation bubbles during production of Ni nanoparticles via pulsed laser ablation in different solvents and their electrocatalytic activity for determination of toxic nitroaromatics, *Chem. Eng. J.* 427 (2021), 130970.
- [31] R. Fathima, A. Mujeeb, Enhanced nonlinear and thermo optical properties of laser synthesized surfactant-free Au-Pt bimetallic nanoparticles, *J. Mol. Liq.* 343 (2021), 117711.
- [32] T. Begildayeva, A. Ahn, S.S. Naik, S.J. Lee, J. Theerthagiri, T.H. Kim, M.Y. Choi, Facile one-pot synthesis of CuCN by pulsed laser ablation in nitrile solvents and mechanistic studies using quantum chemical calculations, *Sci. Rep.* 11 (2021) 14389.
- [33] S. Shankar Naik, S.J. Lee, Y. Yu, A.M. Al-Mohaiomed, J. Theerthagiri, M.Y. Choi, Novel approach for the synthesis and recovery of lithium carbonate using a pulsed laser irradiation technique, *Mater. Lett.* 308 (2022), 131218.
- [34] S.H. Lee, H.J. Jung, S.J. Lee, J. Theerthagiri, T.H. Kim, M.Y. Choi, Selective synthesis of Au and graphitic carbon-encapsulated Au (Au@GC) nanoparticles by pulsed laser ablation in solvents: catalytic Au and acid-resistant Au@GC nanoparticles, *Appl. Surf. Sci.* 506 (2020), 145006.
- [35] H. Deng, C. Zhang, Y. Xie, T. Tumlin, L. Giri, S.P. Karna, J. Lin, Laser induced MoS₂/carbon hybrids for hydrogen evolution reaction catalysts, *J. Mater. Chem. A* 4 (2016) 6824–6830.
- [36] G. Wang, H. Wang, X. Lu, Y. Ling, M. Yu, T. Zhai, Y. Tong, Y. Li, Solid-state supercapacitor based on activated carbon cloths exhibits excellent rate capability, *Adv. Mater.* 26 (2014) 2676–2682.
- [37] X. Liu, S. Xi, H. Kim, A. Kumar, J. Lee, J. Wang, N.Q. Tran, T. Yang, X. Shao, M. Liang, M.G. Kim, H. Lee, Restructuring highly electron-deficient metal-metal oxides for boosting stability in acidic oxygen evolution reaction, *Nat. Commun.* 12 (2021) 5676.
- [38] J. Qin, Y. Zhang, D. Leng, F. Yin, The enhanced activity of Pt–Ce nanoalloy for oxygen electroreduction, *Sci. Rep.* 10 (2020) 14837.
- [39] R. Chattot, T. Asset, P. Bordet, J. Drnec, L. Dubau, F. Maillard, Beyond strain and ligand effects: microstrain-induced enhancement of the oxygen reduction reaction kinetics on various PtNi/C nanostructures, *ACS Catal.* 7 (2017) 398–408.
- [40] D. Zhang, C. Zhang, J. Liu, Q. Chen, X. Zhu, C. Liang, Carbon-encapsulated metal/metal carbide/metal oxide core-shell nanostructures generated by laser ablation of metals in organic solvents, *ACS Appl. Nano Mater.* 2 (2019) 28–39.
- [41] J. Theerthagiri, R.A. Senthil, M.H. Buraidah, J. Madhavan, A.K. Arof, M. Ashokkumar, One-step electrochemical deposition of Ni_{1-x}Mo_xS ternary sulfides as an efficient counter electrode for dye-sensitized solar cells, *J. Mater. Chem. A* 4 (2016) 16119–16127.
- [42] H. You, F. Zhang, Z. Liu, J. Fang, Free-standing Pt–Au hollow nanourchins with enhanced activity and stability for catalytic methanol oxidation, *ACS Catal.* 4 (2014) 2829–2835.
- [43] H. Gao, S. Liao, Y. Zhang, X. Jia, L. Zhou, Z. Zheng, Y. Yang, Methanol-tolerant Se/Pt/C: effects of Se content on the structure and electrocatalytic performance for oxygen reduction reaction, *Ionicics* 26 (2020) 1315–1323.
- [44] D. Wang, X. Cui, Q. Xiao, Y. Hu, Z. Wang, Y.M. Yiu, T.K. Sham, Electronic behaviour of Au–Pt alloys and the 4f binding energy shift anomaly in Au bimetallics: X-ray spectroscopy studies, *AIP Adv.* 8 (2018), 065210.
- [45] C. Tan, Y. Sun, J. Zheng, D. Wang, Z. Li, H. Zeng, J. Guo, L. Jing, L. Jiang, A self-supporting bimetallic Au@Pt core-shell nanoparticle electrocatalyst for the synergistic enhancement of methanol oxidation, *Sci. Rep.* 7 (2017) 6347.
- [46] L. Huang, C.Y. Zheng, B. Shen, C.A. Mirkin, High-index-facet metal-alloy nanoparticles as fuel cell electrocatalysts, *Adv. Mater.* 32 (2020), 2002849.
- [47] J. Enkovaara, C. Rosgaard, J.J. Mortensen, J. Chen, M. Dulak, L. Ferrighi, J. Gavnholt, C. Glinsvad, V. Haikola, H.A. Hansen, H.H. Kristoffersen, M. Kuusma, A.H. Larsen, L. Lehtovaara, M. Ljungberg, O. Lopez-Acevedo, P.G. Moses, J. Ojanen, T. Olsen, V. Petzold, N.A. Romero, J. Stausholm-Møller, M. Strange, G. A. Tritsaris, M. Vanin, M. Walter, B. Hammer, H. Häkkinen, G.K.H. Madsen, R. M. Nieminen, J.K. Nørskov, M. Puska, T.T. Rantala, J. Schiøtz, K.S. Thygesen, K. W. Jacobsen, Electronic structure calculations with GPAW: a real-space implementation of the projector augmented-wave method, *J. Phys.: Condens. Matter* 22 (2010), 253202.
- [48] J.P. Perdew, K. Burke, M. Ernzerhof, Generalized gradient approximation made simple, *Phys. Rev. Lett.* 77 (1996) 3865–3868.
- [49] M.K. Agusta, W.A. Dino, M. David, H. Nakanishi, H. Kasai, Theoretical study of hydrazine adsorption on Pt(111): Anti or cis? *Surf. Sci.* 605 (2011) 1347–1353.
- [50] P.-P. Tang, X. Lin, H. Yin, D.-X. Zhang, H. Wen, J.-J. Wang, P. Wang, Hierarchically nanostructured nickel–cobalt alloy supported on nickel foam as a highly efficient electrocatalyst for hydrazine oxidation, *ACS Sustain. Chem. Eng.* 8 (2020) 16583–16590.
- [51] Z. Wang, L. Xu, F. Huang, L. Qu, J. Li, K.A. Owusu, Z. Liu, Z. Lin, B. Xiang, X. Liu, K. Zhao, X. Liao, W. Yang, Y.-B. Cheng, L. Mai, Copper–nickel nitride nanosheets as efficient bifunctional catalysts for hydrazine-assisted electrolytic hydrogen production, *Adv. Energy Mater.* 9 (2019), 1900390.
- [52] C. Mehta, G. Saini, J.M. Abbas, S. Tripathi, Effect of deposition parameters on structural, optical and electrical properties of nanocrystalline ZnSe thin films, *Appl. Surf. Sci.* 256 (2009) 608–614.
- [53] K. Nakamoto, Applications in inorganic chemistry. Infrared and Raman Spectra of Inorganic and Coordination Compounds, Wiley, New York, 2008, pp. 149–354.
- [54] K.W.S. Sing, R.T. Williams, Physisorption hysteresis loops and the characterization of nanoporous materials, *Adsorpt. Sci. Technol.* 22 (2004) 773–782.
- [55] H. Gao, Y. Wang, F. Xiao, C.B. Ching, H. Duan, Growth of copper nanocubes on graphene paper as free-standing electrodes for direct hydrazine fuel cells, *J. Phys. Chem. C* 116 (2012) 7719–7725.
- [56] Y. Zheng, F. He, M. Chen, J. Zhang, G. Hu, D. Ma, J. Guo, H. Fan, W. Li, X. Hu, Mimicking hydrazine dehydrogenase for efficient electrocatalytic oxidation of N₂H₄ by Fe–NC, *ACS Appl. Mater. Interfaces* 12 (2020) 38183–38191.
- [57] L. Yuan, Z. Yan, L. Jiang, E. Wang, S. Wang, G. Sun, Gold–iridium bifunctional electrocatalyst for oxygen reduction and oxygen evolution reactions, *J. Energy Chem.* 25 (2016) 805–810.
- [58] S. Song, H. Zhang, X. Ma, Z. Shao, R.T. Baker, B. Yi, Electrochemical investigation of electrocatalysts for the oxygen evolution reaction in PEM water electrolyzers, *Int. J. Hydrog. Energy* 33 (2008) 4955–4961.

- [59] S. Cherevko, A.R. Zeradjanin, A.A. Topalov, N. Kulyk, I. Katsounaros, K.J. J. Mayrhofer, Dissolution of noble metals during oxygen evolution in acidic media, *ChemCatChem* 6 (2014) 2219–2223.
- [60] M.H. Miles, M.A. Thomason, Periodic variations of overvoltages for water electrolysis in acid solutions from cyclic voltammetric studies, *J. Electrochem. Soc.* 123 (1976) 1459–1461.
- [61] T. Reier, M. Oezaslan, P. Strasser, Electrocatalytic oxygen evolution reaction (OER) on Ru, Ir, and Pt catalysts: a comparative study of nanoparticles and bulk materials, *ACS Catal.* 2 (2012) 1765–1772.
- [62] D. Mladenović, D.M.F. Santos, G. Bozkurt, G.S.P. Soylu, A.B. Yurtcan, Š. Miljanić, B. Šljukić, Tailoring metal-oxide-supported PtNi as bifunctional catalysts of superior activity and stability for unitised regenerative fuel cell applications, *Electrochim. Commun.* 124 (2021), 106963.
- [63] Q. Liang, G. Brocks, A. Bieberle-Hütter, Oxygen evolution reaction (OER) mechanism under alkaline and acidic conditions, *J. Phys.: Energy* 3 (2021), 026001.
- [64] M. Plevová, J. Hnát, K. Bouzek, Electrocatalysts for the oxygen evolution reaction in alkaline and neutral media. a comparative review, *J. Power Sources* 507 (2021), 230072.